A global decoupling technique for subtractive modelling on acoustic and vibration problems

F. Dumortier, V. Meyer, Laurent Maxit

A global decoupling technique for subtractive modelling on acoustic and vibration problems

F. Dumortier[a,b,*], V. Meyer[b], L. Maxit[a]

[a] *Univ Lyon, INSA Lyon, LVA, EA677, 25 bis av. Jean Capelle, 69621 Villeurbanne Cedex, France*
[b] *Naval Group Research, 199 av. Pierre-Gilles de Gennes, 83190 Ollioules, France*

Abstract

The reverse Condensed Transfer Function (rCTF) method is a substructuring approach based on the concept of condensed mechanical receptance and acoustical impedance. Its objective is to predict the vibroacoustic response of a subsystem which was initially part of a global system, from information taken from the global system and the subtracted subsystem which must be removed. This paper proposes an extended formulation to improve the convergence of the rCTF method for subtractive modelling. The fundamentals of the rCTF method have been proposed recently considering only the decoupling interface between the global system and the subtracted subsystem. This approach of decoupling, called the local approach, exhibits some numerical issues. In order to circumvent them, the decoupling interface is extended in this study to account for a second interface, internal to the subtracted subsystem. The numerical performances of this extension, called the global approach, are firstly studied on an academic rod decoupling case which allows parametric studies. Then, a comparison between the local and global approaches is proposed for the scattering problem of an acoustic plane wave by a rigid sphere in an infinite water medium.

Keywords:
Numerical modelling, Substructuring method, Decoupling method, Subtractive modelling, Rod vibrations, Acoustic scattering, Finite Element modelling.

1. Introduction

Numerical methods in vibroacoustics have been widely used over the last decades in order to study complex systems for which analytical solutions are not available. Among them, element-

*Corresponding author
Email address: florent.dumortier@insa-lyon.fr (F. Dumortier)

based methods such as the Finite Element Method (FEM) have become very popular due to their capacity of giving very accurate results. However, they are often limited to the study of complex systems in the low-frequency range due to their substantial computation time. To overcome those frequency limitations, substructuring methods have been developed. Among those methods, one can cite the component mode synthesis, which deals with large structures by dividing them into components described by their eigenmodes, introduced by Hurty [1] and improved considering different methods: Craig and Bampton method [2], component mode substitution method [3], free interfaces methods [4] or hybrid methods [5]. On the other hand, energy-based methods, such as the Statistical Energy Analysis (SEA) [6], which predicts the energy balance between several coupled subsystems, are well indicated to study problems in the high frequency range due to their simplifying assumptions [7, 8] (weak coupling, high modal density, diffuse field). In the mid-frequency range, where the FEM is too computationally heavy to be employed, and where the SEA asumptions are not met, substructuring methods based on admittance (or receptance) concepts have emerged as an analogy between mechanical and electrical systems [9]. These methods, based on frequency transfer functions, give the possibility to couple subsystems which are characterised by different means: analytical, numerical, experimental ([10, 11]). They were then used by Bishop and Johnson [12] to obtain the receptances, the principal modes and the frequency response of systems consisting in two sub-systems linked at a single or several points. Petersson and Plunt [13, 14] introduced the concept of effective mobilities for multi-point coupled structures, and Kim and Brennan [15] extended the method to structural-acoustic systems with weak coupling.

More recently, the concept was extended to subsystems that are coupled along a line or a surface. The Patch Transfer Function (PTF) approach was developped to couple two acoustic domains [16]. The coupling surface is decomposed into elementary surfaces called patches with a wavelength based criterion. From the patch transfer functions (PTFs) defined and calculated for each uncoupled domain, and considering the superposition principle for linear passive systems, the response of the coupled acoustic domain can be deduced. This method has been extensively studied for various applications [17–22]. In particular, the convergence of the method was improved by introducing residual mode shapes in the modal expansion of the PTFs [23] and by partitioning the subsystems outside the acoustic near field of the structures [24], hence extending the method for the acoustic radiation of structures immersed in a heavy fluid. The Condensed Transfer Function (CTF) method was then proposed as a generalization of the PTF method for partitioning linear

vibro-acoustic problems along line or surface junctions [25]. Instead of considering patches, condensation functions that can take numerous forms (complex exponentials, Chebyshev polynomials) are defined at the coupling interface and are used as an approximate basis for describing the forces and displacements at the junction. Following the study of non-periodically stiffened cylindrical shells using the Circumferential Admittance Approach (CAA), which can be considered as a particular case of the CTF approach for axisymmetric systems using exponentials as condensation functions [26], the influence of non-axisymmetric internal structures on the vibroacoustic behavior of the shell was studied [27, 28]. The convergence of the method was improved with complex exponentials as condensation functions by establishing an optimized piecewise convergence criterion [29]. This allowed applying the CTF method to study the transmission loss of double skin façades [30].

Instead of coupling subsystems as it is usually considered in substructuring approaches, we are interested in this paper in decoupling a subsystem from a global system. This type of decoupling approach has already been considered in the past for point-coupled mechanical systems. The inversion of the coupling problem was first derived by Soedel and Soedel [31] to remove unwanted parts of an automotive suspension system when measuring its transfer functions. From a modelling point of view, the reverse receptance approach (RRA) was proposed to estimate the normal modes of different kinds of plates with holes [32, 33] or grooved plates [34]. The latter were simulated by removing simply supported beams from the flat plate. It was shown that the size of the removed system plays a key role on the convergence of the method. The width and the depth of the grooves should not exceed 3.6% of the plate width and half of the plate thickness, respectively.

Later on, decoupling procedures have been investigated by D'Ambrogio and Fregolent in the framework of experimental investigations, to identify subsystems that cannot be studied separately but only when coupled to other structures [35]. To this end, they estimated the FRFs of the part of interest from the measurement of the FRFs of the global large system and a Finite Element model of a second, residual subsystem. It was highlighted that, for frequencies close to the natural frequencies of the known subsystem, the considered matrices may be ill-conditioned, leading to potential errors in the decoupling [36]. To circumvent this issue, the definition of the subsystem interface was extended by considering internal degrees of freedom (DoFs) of the residual subsystem [37]. An application of the extended interface was proposed on a two-speed transmission system. In this system, the interface DoFs corresponded to the contact gear between the subsystems, while the internal DoFs could be chosen between the gears of the residual subsystem which were not con-

nected to the subsystem of interest. Following this work, a so-called dual approach to substructure (dis)assembling was proposed [38]. Different equilibrium and continuity conditions were imposed during the decoupling process, both in the physical and modal space, and the performances of the different techniques were compared. It must be noted that these approaches were all experimentally oriented, and the FRFs used to perform the decoupling were measured at different points on discrete structures. The approach described in the previously cited papers was then applied to predict the updated FRFs of a thin-walled structure during machining [39]. This study differs from the previous ones by being numerically oriented, as the time-varying FRFs of the workpiece are predicted from FEM models of the initial structures. However, the focus of this study is directed towards reducing the order of the FEM models rather than the definition of the extended interface and the choice of internal DoFs to avoid the numerical instabilities at the anti-resonance frequencies of the subtracted subsystem. A regularization technique based on a singular value decomposition was used to circumvent this numerical issue.

Recently, the present authors have developed the reverse Condensed Tranfer Function (rCTF) method, as a reverse formulation of the CTF method to study the decoupling of vibroacoustic systems using subtractive modelling [40]. The theoretical fundamentals of the rCTF method have been exposed, and the method was validated in the case of a rigid sphere immersed in water and impacted by a plane wave. The model was obtained by decoupling a water filled sphere from an infinite water medium, and the condensed transfer functions (CTFs) necessary to apply the method were computed using analytical models. It was observed that numerical instabilities occur for frequencies around the anti-resonance of the water sphere, following the observations previously drawn [36]. Then, the sensitivity of the method to model errors was studied in a subsequent conference paper [41], by using numerical models to compute the CTFs. The numerical instabilities observed with the analytical models were amplified by the use of numerical models, leading to consequent errors around the anti-resonances of the water filled sphere. In order to circumvent this issue, an alternative decoupling approach is explored in this paper. Instead of considering only the physical decoupling interface between the global system and the subtracted subsystem as it was done in the previously cited papers, a second decoupling interface, internal to the subtracted subsystem, is considered. This approach is similar to the extended interface method proposed in [37–39]. However, there is an important difference lying in the fact that it is aimed at being applied on continuous systems rather than discrete ones, meaning that the internal decoupling interface can be located

anywhere in the subtracted subsystem, when the internal DoFs in the cited articles corresponded to discrete points where measurement could be performed [37, 38], or to selected nodes of the FEM models [39]. As a consequence of the proposed approach, the internal decoupling boundary can take any shape, and a small residual subsystem will result of the decoupling. The influence of this residual subsystem is of paramount importance on the performances of the decoupling approach and will be discussed in this paper. In the following, this numerical process, still based on the rCTF formulation, will be called the global decoupling approach, as opposed to the previous local approach where the decoupling interface is limited to the local boundary between the global system and the subtracted subsystem.

To investigate the differences of performance of the local and global decoupling approaches, a simple case study will be considered at first, consisting in the decoupling of vibrating rods. For this particular case of point decoupling between the one dimensional (sub)systems, the rCTF formulation [40] at the decoupling interface is reduced to the RRA approach [32]. In Section 2, the numerical convergence of the local decoupling approach is studied. In particular, significant errors will be observed around the anti-resonances of the subtracted rod. A sensitivity analysis based on a simple formula for this academic case will allow highlighting the reasons of these discrepancies. Then, in Section 3, the concept of global decoupling approach is introduced and its performances are studied on the same case than for the local approach, to ease the comparison. The influence of the choice of internal interface and of the residual rod will be investigated, and a general criterion for this choice will be proposed to allow applying, theoretically, this approach to any system. Finally, in Section 4, the global subtractive modelling approach will be applied to the rCTF method for the 3-D problem studied in [40], consisting in the scattering of an acoustic plane wave by a rigid sphere immersed in an infinite water medium. For this numerical study, the Condensed Transfer Functions (CTFs) of the (sub)systems will be estimated from numerical models. This will allow studying the propagation of the numerical errors in the proposed global decoupling process.

2. Analysis of the numerical performances of the local decoupling approach

At first, the difference of performances between the local and global subtractive modelling approaches will be evaluated on a simple academic test case. It consists in studying the decoupling of a master rod by a subtracted rod to derive the receptance of the target rod at the decoupling point. The subtractive modelling method used to perform this study is the RRA, as introduced in [32].

The local approach of decoupling will be addressed in Section 2, while Section 3 will be dedicated to the global approach. The principle of local decoupling as well as the related decoupling formula are reminded in subsection 2.1, before analyzing its numerical results in subsection 2.2.

2.1. Local approach of rod decoupling and its formulation

Let us consider three vibrating elastic rods, as shown in Figure 1, only subjected to traction and compression. The rod 1+2 consists in the assembling of the rods 1 and 2. One of its ends is supposed clamped whereas the other one is free. The objective of the local decoupling problem, illustrated in Figure 1b, is to obtain the receptance α_{11} of the rod 1 at point 1, from the receptances μ_{11} and β_{11} of the rods 1+2 and 2, respectively, at the same point.

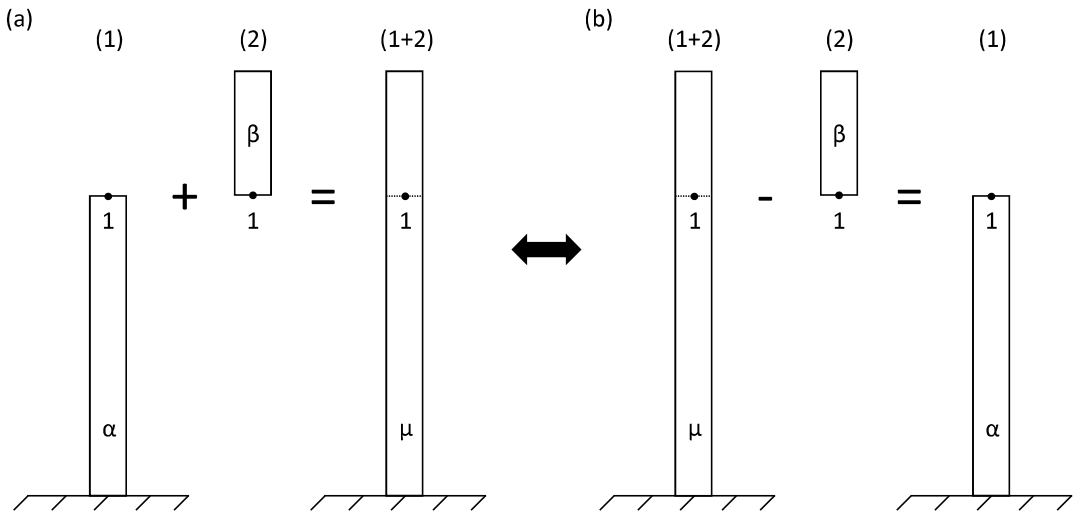

Figure 1: (a) Local coupling. (b) Local decoupling.

It is reminded that the receptance of the rod 1+2, μ_{ij}, represents the ease of motion of the structure at point i when it is subjected to a harmonic point force at point j

$$\mu_{ij} = \frac{U_i}{F_j} \tag{1}$$

where F_j is the amplitude of the harmonic longitudinal force applied at point j at the angular frequency ω and U_i is the amplitude of the longitudinal displacement response at point i. One has to keep in mind that μ_{ij} is a complex value, taking into account the phase shift between the force

at point j and the displacement at point i. When the points i and j are the same, the receptance is referred to as "direct receptance" while it is referred to as "cross receptance" when they differ.

Based on the reciprocity principle [42], the receptances are symmetric, which means that they remain the same if the point of excitation and the point of response are exchanged: $\mu_{ij} = \mu_{ji}$. The definition of the receptances, which has been presented here for the master rod is extended for the receptances of the rod 1 and 2, α_{ij} and β_{ij}, respectively.

To carry on with the decoupling problem, the coupling problem, illustrated in Figure 1a, must initially be considered. It consists in assembling the rods 1 and 2 to obtain the receptance μ_{11} of the rod 1+2, as a function of α_{11} and β_{11}. To do so, a harmonic longitudinal force, F_1^{1+2}, is prescribed at point 1 of the rod 1+2. The longitudinal displacement at the same point, U_1^{1+2} should then be evaluated by assembling the rods 1 and 2. As a first step, we consider that the two rods are uncoupled. The longitudinal forces, F_1^1 and F_1^2 are supposed to be applied at point 1 on each of the two rods 1 and 2, respectively. Taking into account the linear vibratory behaviour of the rods, the displacements at point 1 for these two rods can be written

$$\begin{cases} U_1^1 = \alpha_{11} F_1^1 \\ U_1^2 = \beta_{11} F_1^2 \end{cases} \tag{2}$$

As a second step, the displacement continuity and force equilibrium between the two rods at the coupling point yield the following relations

$$\begin{cases} U_1^1 = U_1^2 = U_1^{1+2} \\ F_1^1 + F_1^2 = F_1 \end{cases} \tag{3}$$

Introducing Eq. (2) in Eq. (3), we can deduce

$$U_1^{1+2} = \frac{\alpha_{11}\beta_{11}}{\alpha_{11} + \beta_{11}} F_1 \tag{4}$$

and then the receptance of the rod 1+2 as a function of α_{11} and β_{11} is inferred:

$$\mu_{11} = \frac{\alpha_{11}\beta_{11}}{\alpha_{11} + \beta_{11}} \tag{5}$$

Then, the decoupling problem of Figure 1b is addressed by inverting Eq. (5), to obtain α_{11} as a function of μ_{11} and β_{11}

$$\alpha_{11} = \frac{\beta_{11}\mu_{11}}{\beta_{11} - \mu_{11}} \tag{6}$$

2.2. Analysis of the numerical results

2.2.1. Studied case and receptances evaluation methods

In the following, for the sake of clarity, the rod 1, 2 and 1+2 will be referred to as "target", "subtracted" and "master" rods, respectively. To compute the receptances of the master and subtracted rods, several methods can be considered. In our case of interest, the receptance of the master rod will be computed using an analytical formulation, while the receptance of the subtracted rod will be computed using the FEM. This choice allows evaluating the sensitivity of the decoupling technique when model errors are introduced via the FEM calculation, as it will be investigated in Section 4. The receptance of the target rod obtained via the decoupling formula of Eq. (6) will be compared to an analytical solution of α_{11}.

The mechanical characteristics and dimensions of the nominal rods for the numerical applications are given in Table 1. The structural damping is introduced in the modelling through a complex Young's modulus: $E^* = E(1 + \mathrm{j}\eta)$.

Parameter	**Notation**	**Value**	**Unit**
Young modulus	E	210	GPa
Poisson coefficient	ν	0.3	-
Density	ρ	7800	kg/m^3
Structural damping coeff.	η	0.02	-
Celerity of long. waves	c_t	6020	m/s
Length of the target rod 1	L_1	3	m
Length of the subtracted rod 2	L_2	0.8	m
Length of the master rod 1+2	L_{1+2}	3.8	m
Section of the rods	S	0.05^2	m^2

Table 1: Mechanical characteristics and rods dimensions.

The calculations are performed in the frequency band [100, 10000] Hz, with 2000 values logarithmically spread over the domain in order to describe properly the resonances and anti-resonances

of the rods. For the calculation of β_{11}, the size of the finite elements was 0.1 m in order to satisfy the criterion of at least 6 elements per longitudinal wavelength at 10000 Hz. As for the analytical calculation of μ_{11}, the details of the calculations and the expression of the receptance is given in Appendix A.

2.2.2. Decoupling results

Now that all the parameters for the calculation have been presented, we can observe and analyze the results from the decoupling formula of Eq. (6). The comparison between the result from the decoupling and the analytical calculation of α_{11} is presented in Figure 2a, while the relative error on α_{11} is shown in Figure 2b.

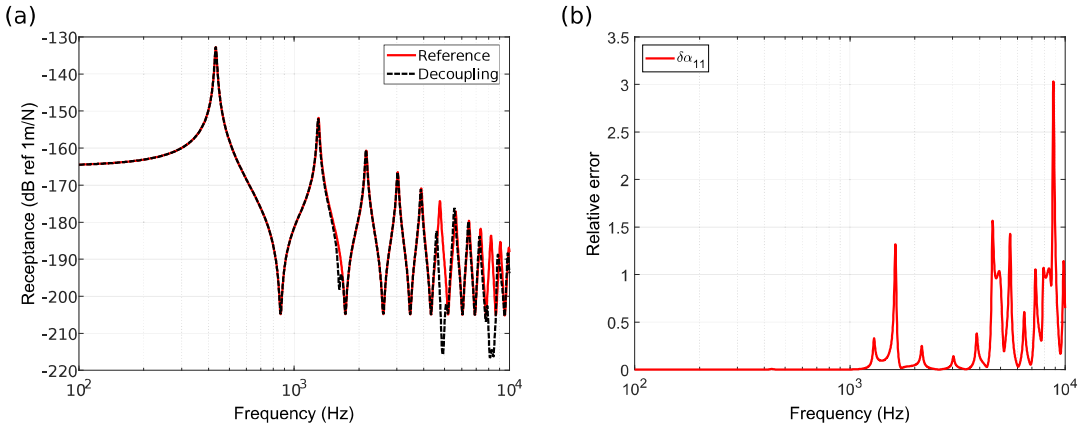

Figure 2: (a) Receptance α_{11} obtained by decoupling. (b) Relative error on α_{11}.

The results show a good fit between the two curves in the main part of the frequency range. Some discrepancies can however be observed around 1600 Hz, 4800 Hz and 8200 Hz, and they appear clearly when looking at the relative error in figure 2b. It is important to mention that, if β_{11} is calculated using an analytical formulation, the results decoupling formula of Eq. (6) do not show those discrepancies, which means that the source of these errors comes from the introduction of model errors via the FE calculation.

2.2.3. Sensitivity analysis

To analyze these errors, one can be interested in deriving the small variations of α_{11} due to the small variations of β_{11} (as there are no errors made on μ_{11})

$$\delta\alpha_{11} = -\frac{\mu_{11}^2}{(\beta_{11} - \mu_{11})^2}\delta\beta_{11} \tag{7}$$

Let's define, for each frequency, the coefficient γ as the ratio between β_{11} and μ_{11}, so that $\beta_{11} = \gamma\mu_{11}$. The error on α_{11} can be rewritten:

$$\delta\alpha_{11} = -\frac{1}{(\gamma - 1)^2}\delta\beta_{11} \tag{8}$$

From Eq. (8), we can deduce that there are two critical conditions that induced significant errors on α_{11}:

- as could be expected, the first condition is when the errors on β_{11}, namely $\delta\beta_{11}$, are high.
- the second condition is when γ is close to one, that is to say that the receptances β_{11} and μ_{11} are close to each other.

As it was observed in Figure 2 that the errors on α_{11} are the highest around the three mentioned frequencies (i.e. 1600 Hz, 4800 Hz and 8200 Hz), one could expect that at least one of the two conditions previously evoked are satisfied at these frequencies. The relative error on β_{11} is shown in Figure 3a, while the receptances β_{11} and μ_{11} are plotted in Figure 3b. As a comparison, the receptance β_{11} is presented for the two calculations (analytical and FE modelling), while only the analytical value is presented for the receptance μ_{11}.

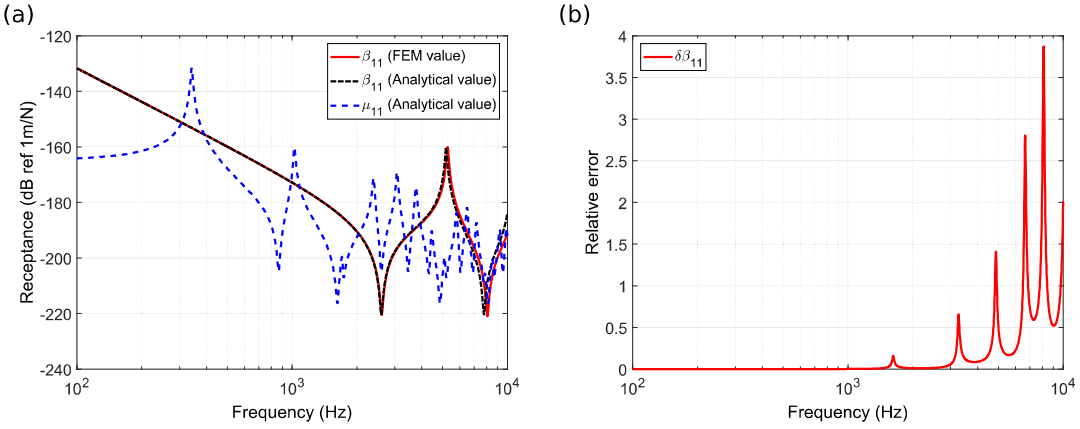

Figure 3: (a) Relative error on β_{11}. (b) Comparison between β_{11} and μ_{11}.

From the results shown in Figure 3, we can deduce that the two critical conditions are indeed satisfied at the three incriminated frequencies. The model errors on β_{11} are significant around the resonances and anti-resonances of the rod due to a slight frequency shift between the analytical calculation and the FE calculation. It is also important to mention that the relative errors exhibit quite high values, which means that the hypothesis a small variations to compute Eq. (7) is not satisfied here. Nevertheless, the analysis drawn from this formula remain satisfying.

More interestingly, we can observe in Figure 3b that, regarding the second critical condition (i.e. μ_{11} and β_{11} are close or equal), the frequency domains at which this condition is satisfied correspond to the anti-resonances of the subtracted rod, which are common to some of the anti-resonances of the master rod. This result can therefore be linked to the previous observations concerning the sources of errors in subtractive modelling: the model errors introduced with the FEM calculation amplify the errors around the anti-resonances of the subtracted subsystem, as it was observed in [41].

This observation, linked to the ones already drawn in previous studies [36, 40, 41], highlights an intrinsic property of local decoupling procedures, which are particularly sensitive to model errors around the anti-resonances of the subtracted subsystem. This means that, in order to look for solutions to circumvent this issue, using this simple rod case study seems like a suitable starting point. Therefore, the possibility of an other decoupling strategy will be investigated in the next section.

3. Analysis of the numerical performances of the global decoupling approach

3.1. Principle of the global decoupling approach

The objective here is to find another way to express α_{11} with information regarding the master and subtracted rods, and without changing the parameters of the initial rods. To do so, a new decoupling strategy will be explored, called the global approach. It is illustrated in Figure 4 for the rod problem. The principle of this approach is to decouple the subtracted rod at an intermediary position of the master rod instead of at its extremity. This decoupling will separate the rod 1 into two rods: the clamped rod which is of interest (still referred to as "target" rod), and a remaining free-free rod, which will be referred to as "residual" rod in the following. As the presence of the residual rod does not affect the dynamic behavior after the decoupling procedure, the global approach is an

alternative formulation to yield the quantity of interest in this study (i.e. the receptance at point 1).

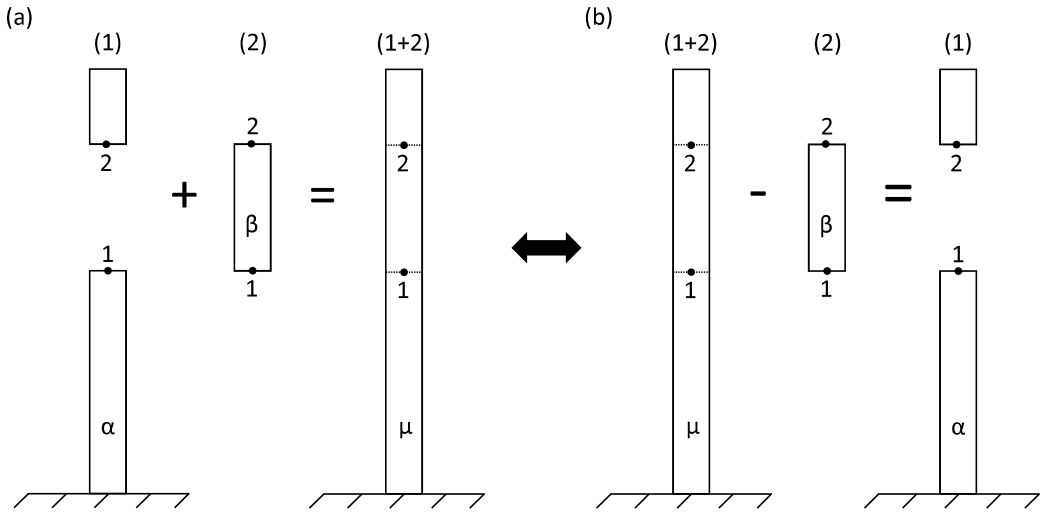

Figure 4: (a) Global coupling. (b) Global decoupling.

This second decoupling approach will then exhibit two coupling points, which means that each rod must now be characterized by a receptance matrix, to account for the direct receptances at points 1 and 2, and for the cross receptance between those two points

$$\mathbf{A} = \begin{bmatrix} \alpha_{11} & \alpha_{12} \\ \alpha_{12} & \alpha_{22} \end{bmatrix}, \qquad \mathbf{B} = \begin{bmatrix} \beta_{11} & \beta_{12} \\ \beta_{12} & \beta_{22} \end{bmatrix}, \qquad \mathbf{M} = \begin{bmatrix} \mu_{11} & \mu_{12} \\ \mu_{12} & \mu_{22} \end{bmatrix}, \tag{9}$$

It must be stressed out that we are still, in this study, interested in obtaining α_{11} only. To do so, as it was done for the local approach, the coupling problem must firstly be considered. This is illustrated in Figure 4a. A unitary harmonic longitudinal force is prescribed successively at the two coupling points. Let us suppose at first that this force is applied at point 1. The force vector is then defined by

$$\mathbf{F} = \begin{bmatrix} 1 \\ 0 \end{bmatrix} \tag{10}$$

The displacement vectors (containing the displacements at the coupling points) associated to

the two uncoupled rods can be written as a function of the receptance matrices and the force vector (considering the superposition principle for linear passive systems). On the other hand, the displacement continuity and force equilibrium at the junction can be written with the displacement and force vector quantities. It yields

$$\begin{cases} \mathbf{U_1} = \mathbf{A}\mathbf{F_1} \\ \mathbf{U_2} = \mathbf{B}\mathbf{F_2} \\ \mathbf{U_{1+2}} = \mathbf{U_1} = \mathbf{U_2} \\ \mathbf{F} = \mathbf{F_1} + \mathbf{F_2} \end{cases} \tag{11}$$

where $\mathbf{U}_\zeta$ represents the displacement vector of rod ζ, and $\mathbf{F}_\zeta$ corresponds to the applied force vector on rod ζ (ζ stands for 1, 2 or 1+2). The resolution of this system of equations gives

$$\mathbf{U_{1+2}} = \mathbf{A}(\mathbf{A}+\mathbf{B})^{-1}\mathbf{B}\mathbf{F} \tag{12}$$

$\mathbf{U_{1+2}}$ contains the displacements at the coupling points for the master rod when excited by a unit point force at point 1. It corresponds then to the first column of the receptance matrix $\mathbf{M}$ of the master rod. Repeating the process for a force applied at point 2, we deduce the expression of the receptance matrix $\mathbf{M}$

$$\mathbf{M} = \mathbf{A}(\mathbf{A}+\mathbf{B})^{-1}\mathbf{B} \tag{13}$$

As in Section 2, the decoupling problem is derived from the coupling problem by inverting Eq. (13). The receptance matrix $\mathbf{A}$ of the rod 1 is then written

$$\mathbf{A} = \mathbf{B}(\mathbf{B}-\mathbf{M})^{-1}\mathbf{M} \tag{14}$$

It can be noted that the expression in Eq. (14) has the same form as in Eq. (6), with matrices instead of single point values. More interestingly, it is the same type of expression as the one obtained for the rCTF approach in [40] to compute the condensed impedances of the target subsystem.

The results from the global decoupling approach will be presented with the same calculation parameters as in Section 2. Concerning the length of the different rods of interest, the position of the first coupling point as well as the length of the master rod remain unchanged in comparison with the local approach, in order to keep the comparison between the local and global approaches relevant. The size of the four rods of interest are given in Table 2.

Parameter	Notation	Value	Unit
Length of the target rod	L_{11}	3	m
Length of the residual rod	L_{12}	0.3	m
Length of the subtracted rod 2	L_2	0.5	m
Length of the master rod 1+2	L_{1+2}	3.8	m

Table 2: Rods dimensions for the global approach.

3.2. Decoupling results

As for the local approach, the decoupling calculation of Eq. (14) was performed by considering an analytical formulation for the receptances of the master rod (see Appendix A) and a FEM computation for the receptances of the subtracted rod.

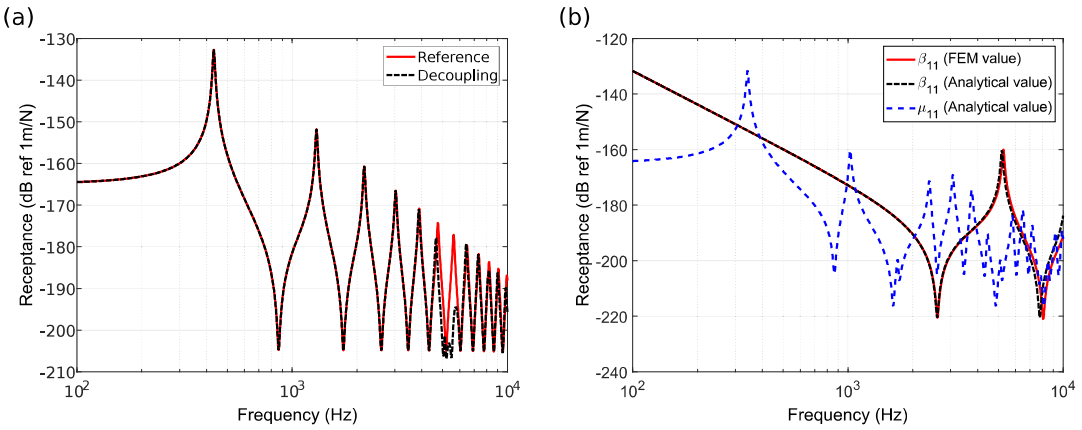

Figure 5: (a) Result of the global decoupling for α_{11}. (b) Amplitude of the receptances β_{11} and μ_{11}.

The result of this calculation is proposed in Figure 5a, and it can be observed that, contrary to the local approach, there is only one frequency domain which exhibits errors, around 5500 Hz. Furthermore, when looking at the amplitude of the receptances μ_{11} and β_{11} in Figure 5b, this frequency domain seems to correspond to the resonance of the subtracted rod instead of its anti-resonance. Besides, one can also observe that, for this calculation, the anti-resonances of the subtracted rod are not necessarily coincident to anti-resonances of the master rod.

The decoupling formula of Eq. (14) involves the inversion of the matrix $\mathbf{B} - \mathbf{M}$. This inversion can amplify the numerical discrepancies related to the model errors and lead to the errors observed

in Figure 5a. The sensitivity of this matrix inversion to numerical errors can be characterized by the condition number, which corresponds, for a normal square matrix, to the ratio between the highest of the two eigenvalues of the matrix over the lowest one [43]

$$\kappa(\mathbf{A}) = \frac{|\lambda_{max}(\mathbf{A})|}{|\lambda_{min}(\mathbf{A})|} \tag{15}$$

where $\mathbf{A}$ is the considered matrix, κ its condition number, and λ_{max} and λ_{min} its maximal and minimal eigenvalues, respectively.

It has already been highlighted in [40] that the ill-conditioning of the inverted matrix around the anti-resonances (for the local approach) of the subtracted subsystem constitutes an important factor for the amplification of the errors. The condition number of the receptance matrices $\mathbf{B}$, $\mathbf{M}$, and $\mathbf{B}-\mathbf{M}$, are shown in Figure 6a. The relative error on α_{11} is also presented in Figure 6b, in order to investigate the relation between a potentially high condition number of the inverted matrix $\mathbf{B}-\mathbf{M}$ and a significant relative error on α_{11}. As there are no apparent errors below 1000 Hz in Figure 5a, the curves in Figure 6 are plotted only above 1 000 Hz for a better clarity.

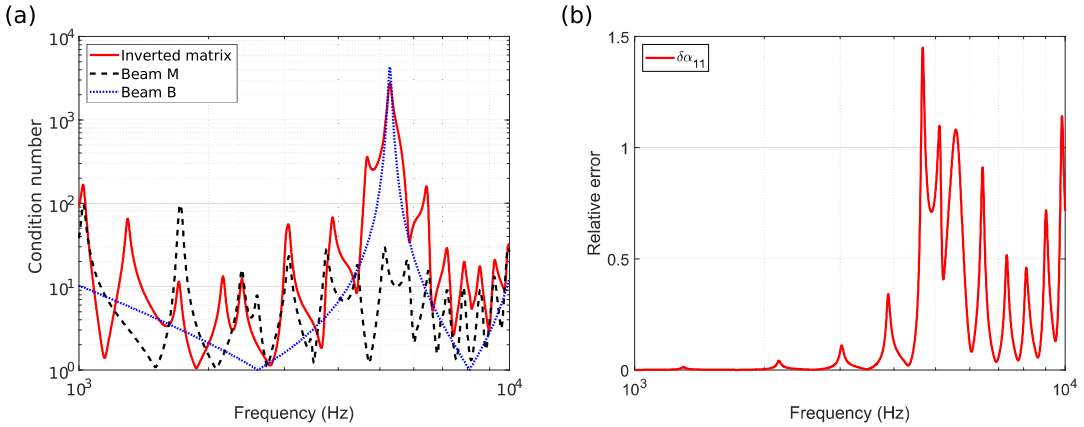

Figure 6: (a) Condition number of the receptance matrices. (b) Relative error on α_{11}.

The red curve displayed in Figure 6a, corresponding to the inverted matrix, shows that there is a frequency domain between 4600 Hz and 6500 Hz where the condition number is relatively high (i.e. greater than 100). This high condition number can be associated to the ill-conditioning of the matrix $\mathbf{B}$ for frequencies close to the resonant frequency, 5271 Hz (see the blue curve). In addition, as previously shown in Section 2, model errors on the receptances of the subtracted rod are the

most significant at the resonances and anti-resonances of the rod. As a result, the ill-conditioning of the inverted matrix amplifies the model errors committed on the receptances of the subtracted rod at frequencies close to its resonances. This may explain the important relative errors on α_{11} in Figure 6b in the frequency band [4600 6500] Hz. For frequencies higher than 6500 Hz, the relative errors observed in Figure 6b remain significant. However, these errors can be associated to slight frequency shifts in the prediction of α_{11} as it can be observed in Figure 5a.

The results exposed in this part show that the global decoupling approach tends to produce less errors than the local decoupling approach. One could think that this is due to the smaller size of the subtracted rod, but it was also observed a change in behavior in the decoupling, as the errors are now located around the resonances of the subtracted rod, instead of its anti-resonances. This could mean that, when considering the global approach, the subtracted rod may not be the only subsystem having an impact on the decoupling performances. Therefore, in the next paragraph, the influence of the residual rod will be investigated.

3.3. Influence of the residual rod

In order to investigate the influence that the residual rod has on the results given by the global approach, a new set of calculations is performed. The position of the first coupling point remains unchanged compared to the two previous studies, and the size of the subtracted rod is fixed to L_2=0.8 m as in Section 2 related to the local approach, in order to get rid of the influence of the size of the subtracted rod. This also allows observing several resonances (i.e. 3264 Hz and 6651 Hz) and anti-resonances (i.e. 1624 Hz, 4941 Hz and 8433 Hz) of the subtracted rod in the frequency range of interest. This means that the only parameter which varies here is the length of the residual rod (and subsequently the length of the master rod), which will be varying logarithmically between 1 cm and 1.5 m.

The results from this study are shown in Figure 7 in terms of condition number of the inverted matrix $\mathbf{B} - \mathbf{M}$ (Figure 7a) and relative error on α_{11} (Figure 7b). The resonances of the subtracted rod are highlighted by the red dashed lines, while the white dashed lines specify the resonances of the residual rod. The first observation we can draw from these figures is that the maxima of condition number and relative error remain located around the resonances of the subtracted rod, regardless of the length of the residual rod. This confirms a major difference between the local and global approaches, as the case when L_{12}=1 cm (i.e. very small residual rod), is very close to the

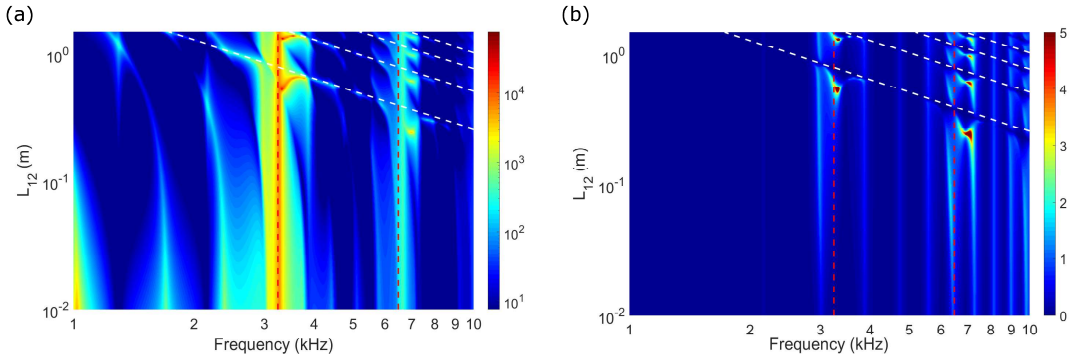

Figure 7: (a) Condition number of the receptance matrices. (b) Relative error on α_{11}.

problem considered in Section 2.

Besides, it can be observed in Figure 7b that the diagonal patterns which tend to appear following the maxima of relative errors are parallel to the resonances of the residual rod (see the white dashed lines). This means that there is a correlation between the errors of the global decoupling technique and the presence of resonances of the residual rod. Subsequently, the relative error made by the global decoupling process tends to decrease as soon as there isn't any more resonance of the residual rod in the frequency range. This statement can be considered as a general criterion that must be met when the global decoupling approach is considered, in order to optimize its performances.

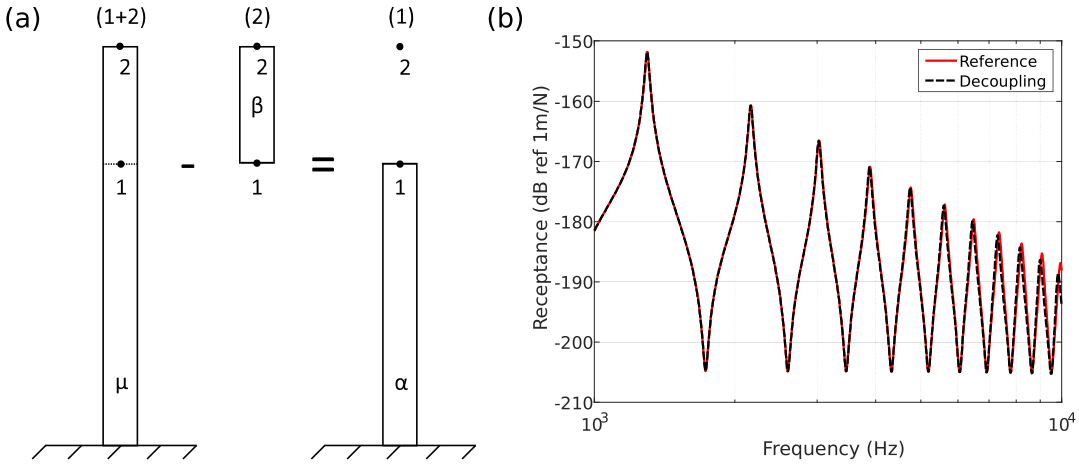

Figure 8: (a) Asymptotic global decoupling scheme. (b) Asymptotic global decoupling result.

This also means that, theoretically, the asymptotic case of this approach, $L_{12} \to 0$, where there

isn't any residual rod anymore (as for the local decoupling approach), would produce the best results. This is verified in Figure 8b where the result of the global decoupling approach is presented for the asymptotic case illustrated in Figure 8a. This result shows that, for the exact same case of decoupling, the global approach produces much better results than the local approach, and this is due to the fact that a second decoupling point has been considered for the formulation. The only remaining errors correspond to the slight frequency shifts related to the FE model of the subtracted rod.

This study on the decoupling of rods has shown us that the global decoupling approach exhibits a better numerical convergence than the local decoupling approach. This improvement is made possible by the fact that the later one needs more information than the former one regarding the receptances of the master and subtracted rods. Furthermore, it has been shown that, by choosing *a priori* the location of the second decoupling interface, we can improve the performances of the global approach. We can now apply it to the scattering of a plane wave by a rigid sphere and compare the accuracy of the prediction with the local approach (already studied in [40, 41]). This study will be investigated in the next Section.

4. Application of the global rCTF approach to predict the scattering of a plane wave by a rigid sphere

We are now interested in applying the global decoupling approach to the rCTF method, in order to strengthen its performances. To do so, the test case consisting in studying the scattering of a plane wave by a rigid sphere immersed in water will be considered. Indeed, as it has already been investigated in previous studies [40, 41], it can constitute a relevant point of comparison to assess the performances of the global approach. The principle of the global approach applied to this test case is illustrated in Figure 9. An infinite water domain with an incident acoustic plane wave (i.e. the master system 1+2) is considered, from which a hollow water sphere (i.e. the subtracted subsystem 2) is subtracted. As a result, we obtain subsystem 1, which is composed of a rigid sphere impacted by the plane wave (the target subsystem) and of a small water filled sphere (the residual subsystem, which does not have an influence on the quantity of interest, the pressure field scattered by the rigid sphere). This study aims at predicting the response at any point of the target subsystem, and not only at the decoupling interface as in Sections 2 and 3. From what was observed in Section 3, the location and size of the residual subsystem will play a key role in the convergence of the results.

Concerning its location, the small residual sphere can be placed theoretically anywhere in the water filled sphere, and it will be placed in this case at its center. As for the size of the residual sphere, following the criterion proposed in 3, it is chosen small enough to avoid having any resonance in the frequency range of the study. The geometrical and material characteristics of the studied system are summerized in Table 3, and the calculations will be carried out between 100 Hz and 1000 Hz.

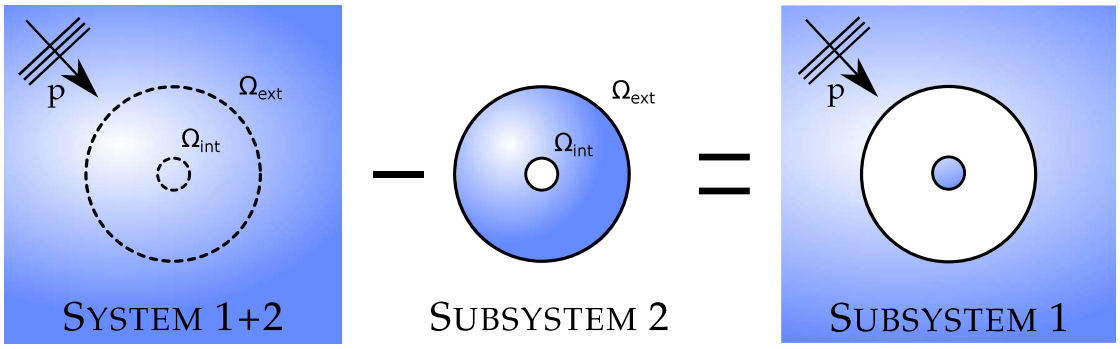

Figure 9: Global rCTF approach applied to the scattering of a plane wave by a rigid sphere.

Parameter	**Notation**	**Value**	**Unit**
Exterior radius	R_{ext}	1	m
Interior radius	R_{int}	0.1	m
Density	ρ	1000	kg.m^{-3}
Sound speed	c_0	1500	m.s^{-1}
Loss factor	η	0.001	-

Table 3: Material and geometrical characteristics of the system.

The theoretical fundamentals of the rCTF method will firstly be recalled in Subsection 4.1, then the procedure to compute the condensed quantities from the numerical models will be addressed in Subsection 4.2, and finally the results from the global rCTF approach on this test case will be presented and discussed in Subsection 4.3.

4.1. Theoretical fundamentals of the rCTF method

The decoupling problem illustrated in Figure 9 can be addressed by using the rCTF method, for which the theoretical developments have been explained in details in [40]. The objective of the

method is to obtain the response at any point of the target subsystem, and the main steps to reach this aim will be recalled in this paragraph.

Let us consider two systems (subsystems 1 and 2) initially coupled along two surfaces, Ω_{ext} and Ω_{int}. A set of N orthonormal functions, called condensation functions, is defined on Ω_{ext} and Ω_{int}: $\{\varphi^i\}_{1\leqslant i\leqslant N}$. Then, the pressures p_α and normal velocities u_α on Ω_{ext} and Ω_{int} can be approximated, for each sub-system α, as a linear combination of the condensation functions

$$\left\{\begin{array}{l} p_\alpha(r,\theta,\phi) \simeq \sum\limits_{i=1}^{N} P_\alpha^i \varphi^i(r,\theta,\phi) \\ u_\alpha(r,\theta,\phi) \simeq \sum\limits_{i=1}^{N} U_\alpha^i \varphi^i(r,\theta,\phi) \end{array}\right. , \quad (r,\theta,\phi) \in \Omega_{ext} \cup \Omega_{int} \tag{16}$$

where P_α^i and U_α^i are the unknowns. To estimate the unknowns in Eq. (16), condensed transfer functions (CTFs) are defined between φ^i and φ^j for each uncoupled subsystem as

$$Z_\alpha^{ij} = \frac{\langle \bar{p}_\alpha, \varphi^i \rangle}{\langle u_\alpha, \varphi^j \rangle} = \langle \bar{p}_\alpha, \varphi^i \rangle \tag{17}$$

where $\langle \bullet, \bullet \rangle$ is the scalar product, and $\bar{p}_\alpha$ corresponds to the resulting pressure on Ω_{ext} or Ω_{int} when the subsystem is excited by $u_\alpha = \varphi^j$. As the considered problem is here purely acoustical, the CTFs will correspond to condensed impedances (i.e. pressure over velocity). The $N \times N$ condensed impedances matrices $\mathbf{Z_1}$ and $\mathbf{Z_2}$ of subsystems 1 and 2 are then obtained by accounting for all the condensation functions.

Concerning the condensed impedances of system 1+2, the decoupling boundaries Ω_{ext} and Ω_{int} are fictitious ones. A velocity jump should then be prescribed on the decoupling boundaries, hence defining the CTFs as

$$Z_{1+2}^{ij} = \frac{P_{1+2}^i}{\delta U_{1+2}^j} = \frac{\langle \bar{p}_{1+2}, \varphi^i \rangle}{\langle \varphi^j, \varphi^j \rangle} = \langle \bar{p}_{1+2}, \varphi^i \rangle \tag{18}$$

where P_α corresponds to the resulting pressure on Ω_{ext} or Ω_{int} when the system is excited by a prescribed velocity jump.

The decoupling process to obtain $\mathbf{Z_1}$ knowing $\mathbf{Z_{1+2}}$ and $\mathbf{Z_2}$ is similar to the one described in Section 3 related to the global approach of the rod decoupling test case. The coupling problem is initially considered and then reversed. The condensed impedance matrix of the subsystem 1 can then be obtained from the condensed impedance matrices of the system 1+2 and the subsystem 2 [40]

$$\mathbf{Z_1} = \mathbf{Z_2}\left(\mathbf{Z_2} - \mathbf{Z_{1+2}}\right)^{-1}\mathbf{Z_{1+2}} \tag{19}$$

It is worth noticing that this expression is of the same type as in Eq. (14), highlighting the concordance between the two test cases when the global approach is considered. The difference between those two expressions lies in the size of the matrices, as we are now dealing with $N \times N$ matrices instead of 2×2 matrices. Then, following some developments presented in details in [40], the total pressure at any point M in the target subsystem can be expressed as

$$p_1(M) = p_{1+2}(M) + \left(\mathbf{I} + \mathbf{Z_2}\left(\mathbf{Z_2} - \mathbf{Z_{1+2}}\right)^{-1}\mathbf{Z_{1+2}}\mathbf{Z_2}^{-1}\right)\mathbf{P^M_{1+2}}\mathbf{Z_2}^{-1}\mathbf{P_{1+2}} \tag{20}$$

where

- $p_{1+2}(M)$ is the pressure induced by the acoustic plane wave at point M of system 1+2.
- $\mathbf{P_{1+2}}$ is the condensed pressure at the surfaces Ω_{ext} and Ω_{int} of system 1+2 induced by the acoustic plane wave.
- $\mathbf{P^M_{1+2}}$ is the condensed pressure at the surfaces Ω_{ext} and Ω_{int} of system 1+2, induced by a monopole source of unit volume velocity located at point M.

The condensed pressures $\mathbf{P_{1+2}}$ and $\mathbf{P^M_{1+2}}$ correspond to the pressures induced by the considered excitations (acoustic plane wave and monopole source of unit volume velocity, respectively) projected on the condensation function in the sense of the scalar product.

As it was already discussed in Section 2, there are several ways of computing the condensed impedances of the different subsystems of interest. In [40], an analytical formulation was considered in order to assess the validity of the rCTF method. However, analytical approaches are only available for academic cases. An application of the rCTF approach to engineering cases in the future will require the use of numerical methods which will introduce small numerical errors in the evaluation of the CTFs. Then, in the following, the condensed impedances will be computed from numerical models, as it has already been briefly presented in [41], so that the benefits of using the global method to reduce the sensitivity to model errors can be highlighted. The procedure to compute the condensed impedances from numerical models is hence presented in the next paragraph.

4.2. Computation of the CTFs from numerical models

4.2.1. Definition of the condensation functions

In order to compute the condensed impedances from numerical models, the condensation functions must firstly be introduced. In this work, we will consider 2D gate functions, as it is done for the Patch Transfer Function (PTF) approach [24] (a particular case of the CTF approach). These gate functions are defined according to their surface Ω_s

$$\varphi^i(\theta_s, \phi_s) = \begin{cases} \frac{1}{\sqrt{\Omega_s}} & \text{if} \quad \begin{cases} \theta_{i-1} \leqslant \theta_s < \theta_i \\ \phi_{i-1} \leqslant \phi_s < \phi_i \end{cases} \quad , \quad i \in [\![1, N]\!] \\ 0 \quad \text{elsewhere} \end{cases} \tag{21}$$

In practice, using these condensation functions leads to dividing the decoupling interfaces Ω_{ext} and Ω_{int} into a certain amount of elementary surfaces called patches, as illustrated in Figure 10. Each patch is then defined by the coordinates of its boundaries. The division of the decoupling boundary in Figure 10 is shown for Ω_{ext} only, but Ω_{int} is divided in the same way. According to this definition of the condensation functions, the condensed impedances of a system are computed by exciting each patch successively, and then computing the resulting pressure on all the patches, thus building a $N \times N$ condensed impedance matrix.

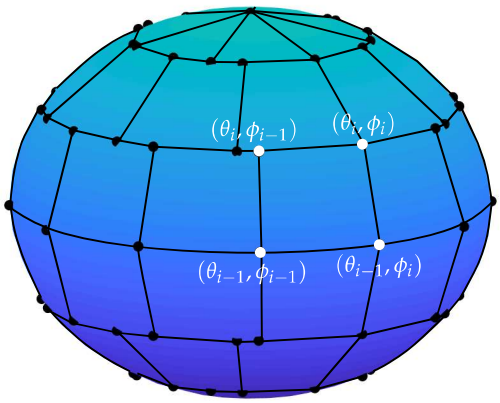

Figure 10: Definition of the condensation functions along the decoupling interface Ω_{ext}.

The size of the patches must follow a wavelength-based criterion in order for the CTF and rCTF methods to give accurate results, and it has already been established in previous studies [16, 25]: the larger patch must be smaller than half the acoustic wavelength at the highest considered frequency

(i.e. 1000 Hz). Following this criterion, each decoupling boundary is divided into 58 patches, which means that the patches belonging to Ω_{int} will be much smaller than the necessary criterion.

4.2.2. Condensed impedances and pressures of the systems

Now that the condensation functions have been defined, the condensed impedances (for both the infinite water medium and the hollow water sphere) and pressures (for the infinite water medium only) can be computed. As it has already be mentioned, those quantities will be computed from numerical models, in order to assess the sensitivity of the global decoupling approach to model errors. The procedure to compute the condensed impedances of the infinite water medium (i.e. system 1+2) and of the hollow water sphere (i.e. subsystem 2), and the condensed pressures in the infinite water medium are developed in details in Appendix B.

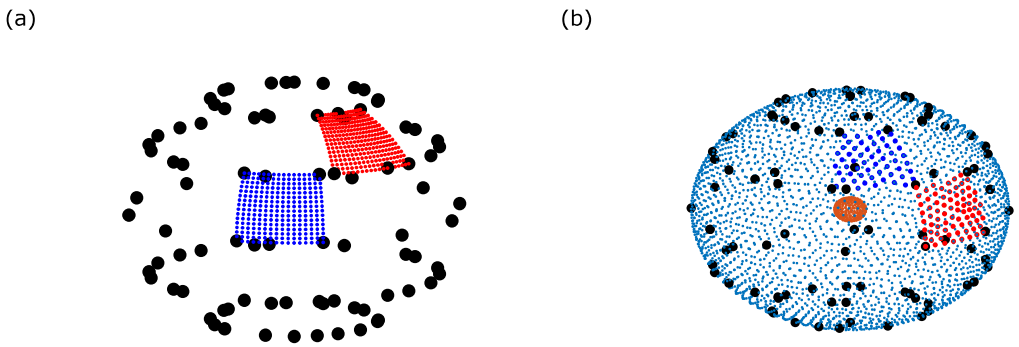

Figure 11: (a) Discretization of the incident and receiving patches to compute $\mathbf{Z_{1+2}}$. (b) Identification of the nodes belonging to the incident and receiving patches to compute $\mathbf{Z_2}$.

To compute the condensed impedances of the infinite water domain, the integral formulation of Eq. (B.1) is considered, as described in Appendix B.1. Each patch is discretized into a certain amount of points, allowing to prescribe the velocity jump on the points belonging to the incident patch, and to estimate the resulting pressure on the points belonging to the receiving patch (see Eq. (B.3)). A similar process is used to evaluate numerically the condensed pressures $\mathbf{P_{1+2}}$ and $\mathbf{P^M_{1+2}}$ (see Eqs. (B.5) and (B.6)). In the following, the size of this discretization has been set to $\delta\theta = \delta\phi = 1°$, as trials have shown that a coarser discretization step would downgrade the results of the rCTF approach. The discretization for a given incident patch and a given receiving patch is

illustrated in Figure 11a. The black dots represent the patches boundaries, while the red and blue dots correspond to the discretization points on which are applied the three previously mentioned equations. Figure 12a shows three examples of condensed impedances of the infinite water medium computed from the numerical formulation described in Appendix B.1 and compared to an analytical computation. The first transfer function (TF) corresponds to a direct condensed impedance (i.e. the incident and receiving patches are the same), the second TF is a crossed impedance between two patches located on Ω_{ext}, and the third TF is a crossed condensed impedance between a patch located on Ω_{ext} and a patch located on Ω_{int}. The good agreement between the analytical and numerical calculations validates the numerical process proposed to evaluate those condensed impedances. Slight differences can be observed, which are the result of the approximations of the numerical process. They can be related to the angular resolution considered in the discrete integral formulation. The influence of these errors on the convergence of the global rCTF approach will be studied in the next paragraphs.

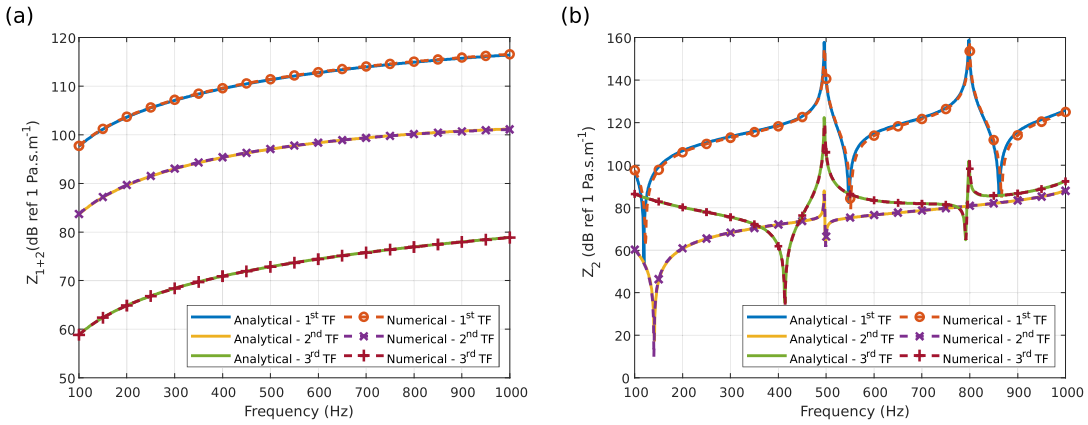

Figure 12: (a) Condensed impedances of the infinite water medium. (b) Condensed impedances of the hollow water sphere.

Concerning the condensed impedances of the hollow water sphere, a FEM formulation is used, as described in Appendix B.3. A FE model of the hollow water sphere is hence constructed, with the size of the elements following a wavelength-based criterion. It is generally admitted that, for acoustic systems, a criterion taking into account between 6 and 10 elements per acoustic wavelength at the highest considered frequency is acceptable. We have seen in Sections 2 and 3 that predicting correctly the resonances and anti-resonances of the systems is of paramount importance for the

convergence of decoupling procedures. In the considered frequency range, the hollow water sphere exhibits two resonances: one at 496 Hz, and one at 798 Hz. There is also one anti-resonance appearing at 833 Hz. To describe accurately those resonances and anti-resonance, 10 elements per acoustic wavelength at the highest considered frequency are then taken into account. The resulting model exhibits 4097 nodes and 22046 second order tetrahedral elements. The nodes at the decoupling interfaces Ω_{ext} and Ω_{int} are shown in Figure 11b, along with the identification of the nodes belonging to a given incident patch and a given receiving patch. The comparison of three condensed impedances computed with this FEM formulation to an analytical calculation is shown in Figure 12b. The first TF is a direct condensed impedance on Ω_{ext}, the second TF is a crossed condensed impedance between two patches located on Ω_{int} and the third TF is a crossed condensed impedance between a patch located on Ω_{ext} and a patch located on Ω_{int}. Once again, we can conclude that the numerical calculation of these condensed impedances is valid, as this figure highlights the correct description of the resonances of the hollow water sphere.

4.3. Application of the global rCTF approach to predict the total pressure in the domain

Once the condensed impedances of the systems of interest have been calculated, the global rCTF approach can be applied to predict the response at any point of the target subsystem using Eq. (20). To do so, the results from the global rCTF approach will be compared to an analytical calculation of the total pressure which can be found in literature [44].

From an extension of the theoretical pressure induced by the plane wave incident in the plane $\theta^i = \pi$ (see Figure 13) in the infinite water medium on the spherical harmonics, and by considering the Helmholtz equation in the medium and the Euler relation at the surface of the sphere, the total pressure in the domain (corresponding to the sum of the incident pressure and the pressure scattered by the rigid sphere) can be obtained from the following expression [44]

$$p_{\text{theo}}(r,\theta) = P_i \sum_{n=0}^{N_{max}} (2n+1)\,\mathrm{j}^n P_n(\cos\theta)\left[j_n(k_0 r) - \frac{j_n'(k_0 R_{ext}) h_n(k_0 r)}{h_n'(k_0 R_{ext})}\right] \tag{22}$$

where P_n is the Legendre polynomial, j_n and j_n' are respectively the spherical Bessel function of the first kind and its derivative, and h_n and h_n' are respectively the spherical Hankel function of the first kind and its derivative. N_{max} corresponds to the number of spherical harmonics taken in the calculation and its value has an important impact on the convergence of the calculation. It has

been observed after trial and error testing that taking $N_{max} = 40$ allows the calculation to correctly converge while keeping a low computing time.

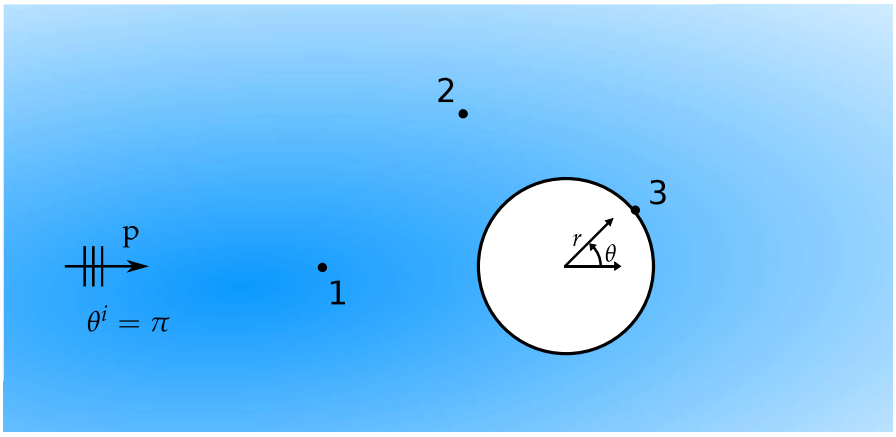

Figure 13: Location of the measuring points and coordinate system.

To study the accuracy of the global decoupling approach based on the rCTF formalism, let us focus on the Frequency Response Functions (FRFs) of the pressure at given points in the domain. This frequency analysis, as performed in Sections 2 and 3, allows identifying potentially problematic frequencies at which the calculation fails to converge. It has been observed in [40], and then in Section 2, that the local decoupling approach is very sensitive to model errors around the common anti-resonances between the master system and the subtracted subsystem. On the other hand, it has been observed in Section 3 that the sensitivity to model errors of the global decoupling approach was higher around the resonances of the subtracted subsystem. To decrease this sensitivity, it is recommended that the residual subsystem should be defined such that no resonance should occur in the frequency range of interest. For the local rCTF calculation, the first two resonances of the full water sphere are located at 497 Hz and 798 Hz, while the anti-resonance appears at 750 Hz. Concerning the global approach, the resonances and anti-resonances of the hollow water sphere were given in paragraph 4.2.2. As for the residual subsystem, which is a water sphere of radius 0.1 m, its first resonance appears at 4969 Hz, which is way outside the considered frequency range.

It must also be stressed out that the result of the global decoupling approach for this test case, when the condensed impedances are computed from analytical model, give the same results as for the local approach, for which the results are presented in [40]. The errors never exceed 1 dB, which

is acceptable from a practical point of view. Those errors can be explained by the fact that the surface of the sphere is approximated into patches, which means that the subtracted subsystem is not exactly a sphere, but an approximated sphere. These calculations will not be shown here as the focus is made on the sensitivity of the global decoupling approach when numerical errors are introduced in the models.

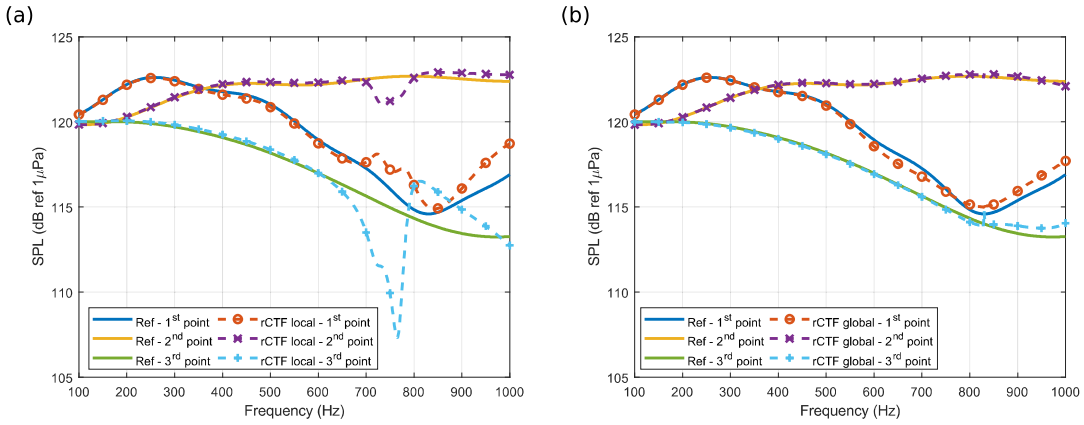

Figure 14: Total pressure at given points of the domain. (a) Local approach ([41]). (b) Global approach.

The FRFs of the total pressure at three different points, which have been chosen in order to account for different distances and angles from the surface of the sphere (see the point locations in Figure 13), are presented in Figure 14a for the local approach and 14b for the global approach. This figure validates the trends concerning the local and global approaches already observed in Sections 2 and 3, as the errors around the anti-resonance of the water sphere (which was located at 750 Hz for the local approach) have been greatly reduced with the global approach. This means that the global rCTF approach is able to deliver better results than the local approach even when the complexity of the studied systems increases.

Let us have a look at the cartographies of the pressure field around the sphere at two frequencies to confirm these correct predictions: at 830 Hz where slight errors appeared in Figure 14b, and at the highest considered frequency (i.e. 1000 Hz), to see if the calculation has correctly converged (as the size of the patches was chosen in order to go up to this frequency). Those cartographies are presented in Figure 15, for the two mentioned frequencies. The comparison is made between the analytical calculation of Eq. (22) (figures on the left) and the global rCTF calculation of Eq. (20)

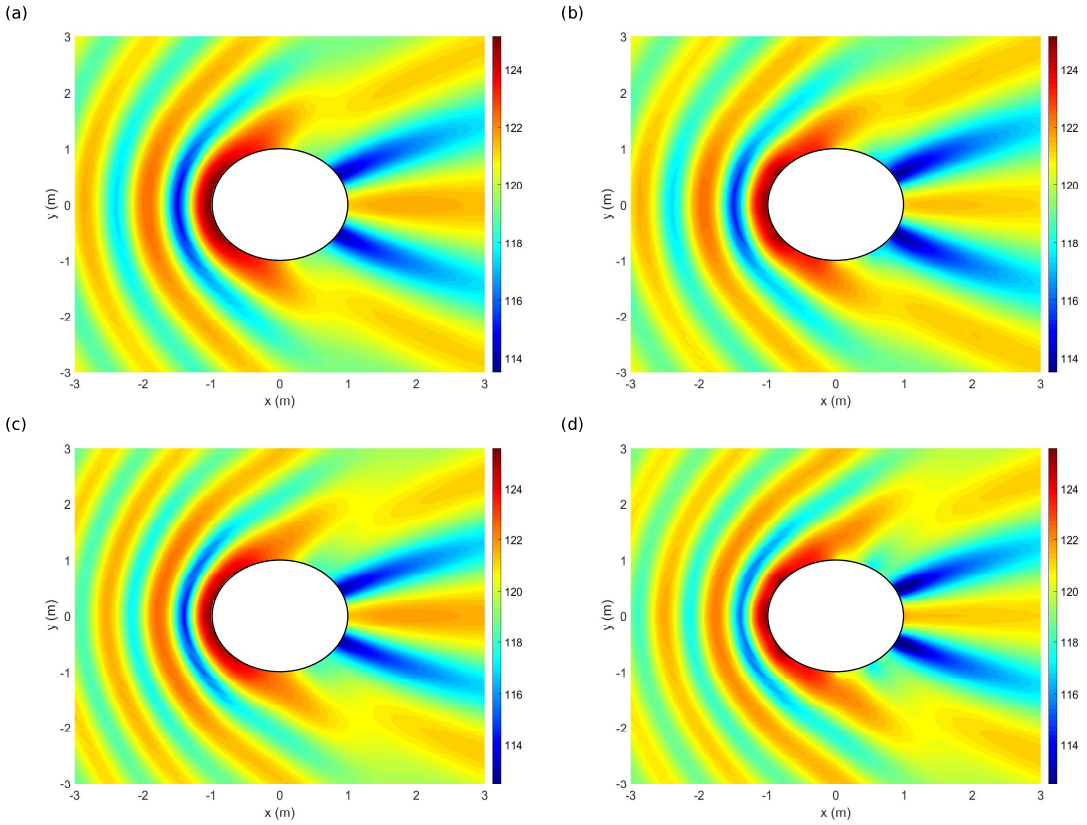

Figure 15: Cartographies of the total pressure in the domain. (a) Reference - 830 Hz. (b) Global rCTF approach - 830 Hz. (c) Reference - 1000 Hz. (d) Global rCTF approach - 1000 Hz.

(figures on the right). There is a very good agreement in general between those two calculations, and for the two specific frequencies. All the maxima and minima of pressure are correctly described, both in terms of localization and amplitude. Some slights differences can be observed on the shadow zones which can be attributed to the fact that the sphere surface is approximated by patches (as shown in Figure 10). Results (not shown here) for other frequencies show also a very good agreement between the 2 calculations. This means that we can ultimately conclude that the global decoupling approach does circumvent the limitations which were observed concerning the local decoupling approach.

It must be noted that some investigations, not presented here for the sake of conciseness, have been done considering a bigger residual sphere comprising resonances in the considered frequency

range. The results from these investigations showed consequent errors precisely located around the resonances of the residual subsystem. As such, the criterion proposed in Section 3 concerning the size of the residual subsystem (i.e. the absence of resonance in the system) has proven to be valid on this test case. This confirms the fact that the size and position of the internal decoupling interface can be chosen *a priori* in order to minimize the decoupling errors.

5. Conclusion

A global decoupling approach has been investigated in this paper, arising from the necessity of circumventing the high sensitivity to model errors of the initial local decoupling approach [40, 41] around the anti-resonances of the subtracted subsystem. This property of the decoupling procedures, already observed in [36, 38], was confirmed in Section 2. In this global approach, a second decoupling interface is considered inside the subtracted subsystem. This approach was, at first, studied on a simple test case consisting in the decoupling of vibrating rods. It was observed that the introduction of the second decoupling interface in the global approach changes the intrinsic behavior of the decoupling scheme, as the errors were then located around the resonances of the subtracted rod. Then, a second analysis showed that the errors practically disappeared as soon as the residual rod was small enough to avoid any resonance in the considered frequency range. This allowed proposing a general criterion for improving the convergence of the global approach.

Given these observations, the global approach was applied to a more complex 3D case consisting in the prediction of the pressure field scattered by a rigid sphere when it is impacted by an acoustic plane wave in an infinite water medium. This system, already studied using the local rCTF approach [40, 41], allowed highlighting the difference of performances between the local and global approaches. It consisted in subtracting to an acoustic model of an infinite water medium, a model of a water sphere (in the case of the local approach) or of a hollow water sphere (in the case of the global approach). The procedure to compute the Condensed Transfer Functions from numerical models of initial (sub-)systems was described in details. A FEM formulation was used to compute the CTFs of the hollow water sphere, while the CTFs of the infinite water medium were calculated from an integral formulation, which has been validated by comparison with analytical results. The total pressure in the domain was then obtained using the equations of the rCTF method, and the observations made with the initial rod case study were found back with this test case, hence validating the interest of the proposed global approach.

Finally, it must be noted that, if the concept of the global approach, consisting in defining an internal decoupling boundary, is similar to the method of the extended interface proposed in [37–39], some key differences can be highlighted between the two approaches. The global approach proposed in this paper is aimed for numerical modelling and based on the calculation of CTFs rather than FRFs. Besides, the approach developed in this paper is aimed at being applied on continuous systems as illustrated by the application in Section 4. As such, the definition of internal interface differs in the fact that its location and size can be chosen during the first stage of model development. This allowed defining *a priori* a criterion concerning the resulting residual subsystem, not considered in the previously cited studies, in order to obtain better results on any investigated system.

Acknowledgments

This work was funded by the French National Research Agency (ANR) within the plan "France Relance", and was performed within the framework of the LabEx CeLyA (ANR-10-LABX-0060) of Université de Lyon, in collaboration with Naval Group Research.

Appendix A. Analytical expressions of the receptances

Appendix A.1. Analytical receptances of the target rod

In order to calculate the receptances of the target rod considered in Sections 2 and 3, a harmonic longitudinal force F is applied on the point 1 of the rod, according to the definition of the receptance in Eq. (1). The equation of motion corresponding to the problem of a longitudinally vibrating rod is given by:

$$ES\frac{\partial^2 U}{\partial x^2} - \rho S\frac{\partial^2 U}{\partial t^2} = 0 \tag{A.1}$$

where U is the displacement of the rod. Considering the stationary response of the rod for a harmonic force of angluar frequency ω, the rod displacement can be written $u(t,x) = U(x)\mathrm{e}^{\mathrm{j}\omega t}$ and Eq. (A.1) becomes:

$$ES\frac{\mathrm{d}^2 U(x)}{\mathrm{d}x^2} + \rho S\omega^2 U(x) = 0 \tag{A.2}$$

The solution of Eq. (A.2) takes the form:

$$U(x) = A\mathrm{e}^{\mathrm{j}kx} + B\mathrm{e}^{-\mathrm{j}kx} \tag{A.3}$$

where k is the wavenumber ($k = \sqrt{\frac{\rho}{E}}\omega = c_t\omega$). The unknown coefficients A and B can be found from the boundary conditions of the rod. As the lower end of the target rod is clamped and the upper end is the point of application of the force, it yields:

$$\begin{cases} U(x=0) = 0 \\ ES\frac{\mathrm{d}U}{\mathrm{d}x}(x = L_{11}) = F \end{cases} \tag{A.4}$$

Injecting the system of Eq. (A.4) into Eq. (A.3), the displacement field along the target rod can be written:

$$U(x) = \frac{F\sin(kx)}{kES\cos(kL_{11})} \tag{A.5}$$

The receptance α_{11} of the target rod can finally be deduced:

$$\alpha_{11} = \frac{U(x = L_{11})}{F} = \frac{\tan(kL_{11})}{kES} \tag{A.6}$$

Appendix A.2. Analytical receptances of the subtracted rod

The receptances of the subtracted rod are computed with a process similar to α_{11}, but the expression will differ due to a change in the boundary conditions. For the calculation of β_{11}, the harmonic longitudinal force is applied on point 1, while the upper end of the rod is free. In order to respect the sign convention adopted for the calculation of α_{11}, the force must be applied in the opposite direction of the force applied on the target rod. The boundary condition then yield

$$\begin{cases} ES\frac{\mathrm{d}U}{\mathrm{d}x}(x=0) = -F \\ ES\frac{\mathrm{d}U}{\mathrm{d}x}(x = L_2) = 0 \end{cases} \tag{A.7}$$

The expression of the receptance is then

$$\beta_{11} = -\frac{1}{kES\tan(kL_2)} \tag{A.8}$$

The receptance α_{22} is the similar to β_{11}, the difference between the two lying in the sign of the receptance, as the applied force will be in the opposite direction. We can directly write

$$\beta_{22} = \frac{1}{kES\tan(kL_2)} \tag{A.9}$$

As for β_{12}, it can be computed by taking the displacement at the end of the rod which is opposite to the point of application of the force. As the receptance are symmetric based on the reciprocity principle [42], either end can be used to carry on with the calculation

$$\beta_{12} = \beta_{21} = \frac{1}{kES\sin(kL_{12})} \tag{A.10}$$

Appendix A.3. Analytical receptances of the master rod

The process for calculating the receptances of the master rod is a bit more complicated than for the two other rods, as the force must now be applied at a point in the middle of the rod. To compute those receptances, the forced wave decomposition technique will be used ([45]).

The rod is separated in two parts at the point of application of the force (which will be point 1 for μ_{11} and μ_{12} and point 2 for μ_{21} and μ_{22}, see Figure 4). The displacement of the lower section of the rod will be referred to as U_1, while the displacement of the upper section of the rod will be referred to as U_2. The process will be shown for a longitudinal force applied on point 1, hence the receptances computed here will be μ_{11} and μ_{12}. The process for μ_{21} and μ_{22} is the same and will not be demonstrated here. One has to keep in mind that, as for the receptances of the subtracted rod, the symmetry of the receptances means that μ_{12} equals μ_{21}.

The displacements of the master rod can be written as:

$$\begin{cases} U_1(x) = A_1 \mathrm{e}^{\mathrm{j}kx} + B_1 \mathrm{e}^{-\mathrm{j}kx}, & x \in [0, L_{11}] \\ U_2(x) = A_2 \mathrm{e}^{\mathrm{j}kx} + B_2 \mathrm{e}^{-\mathrm{j}kx}, & x \in [L_{11}, L_{1+2}] \end{cases} \tag{A.11}$$

where A_1, A_2, B_1 and B_2 are the unknowns. As the rod is clamped at its lower end and free at its upper end, the boundary conditions are:

$$\begin{cases} U_1(x = 0) = 0 \\ ES\frac{\mathrm{d}U_2}{\mathrm{d}x}(x = L_{1+2}) = 0 \end{cases} \tag{A.12}$$

The two other necessary equations to solve the system are given by the displacement continuity and force equilibrium at the point of application of the force:

$$\begin{cases} U_1(x = L_{11}) = U_2(x = L_{11}) \\ \frac{\mathrm{d}U_1}{\mathrm{d}x}(x = L_{11}) - \frac{\mathrm{d}U_2}{\mathrm{d}x}(x = L_{11}) = \frac{F}{ES} \end{cases} \tag{A.13}$$

Hence, by solving the systems of Eq. (A.12) and Eq. (A.13), one can deduce the displacement field in the two sections of the master rod:

$$U_1(x) = \frac{F\sin(kx)}{kES} \cdot \frac{\mathrm{e}^{\mathrm{j}kL_{11}} + \mathrm{e}^{\mathrm{j}k(2L_{1+2}-L_{11})}}{1 + \mathrm{e}^{2\mathrm{j}kL_{1+2}}}, \quad x \in [0, L_{11}] \tag{A.14}$$

$$U_2(x) = \frac{F\sin(kL_{11})}{kES} \cdot \frac{\mathrm{e}^{\mathrm{j}kx} + \mathrm{e}^{\mathrm{j}k(2L_{1+2}-x)}}{1 + \mathrm{e}^{2\mathrm{j}kL_{1+2}}}, \quad x \in [L_{11}, L_{1+2}] \tag{A.15}$$

Finally, the receptances of the master rod can be deduced:

$$\mu_{11} = \frac{\sin(kL_{11})}{kES} \cdot \frac{\mathrm{e}^{\mathrm{j}kL_{11}} + \mathrm{e}^{\mathrm{j}k(2L_{1+2}-L_{11})}}{1 + \mathrm{e}^{2\mathrm{j}kL_{1+2}}} \tag{A.16}$$

$$\mu_{12} = \frac{F\sin(kL_{11})}{kES} \cdot \frac{\mathrm{e}^{\mathrm{j}k(L_{11}+L_2)} + \mathrm{e}^{\mathrm{j}k(2L_{1+2}-(L_{11}+L_2))}}{1 + \mathrm{e}^{2\mathrm{j}kL_{1+2}}} \tag{A.17}$$

Following the same process, the final receptance μ_{22} is given by:

$$\mu_{22} = \frac{F\sin(k(L_{11}+L_2))}{kES} \cdot \frac{\mathrm{e}^{\mathrm{j}k(L_{11}+L_2)} + \mathrm{e}^{\mathrm{j}k(2L_{1+2}-(L_{11}+L_2))}}{1 + \mathrm{e}^{2\mathrm{j}kL_{1+2}}} \tag{A.18}$$

Appendix B. Numerical calculation of the condensed impedances and pressures

To apply the global rCTF approach in Section 4, the condensed impedances $\mathbf{Z_{1+2}}$ and $\mathbf{Z_2}$, as well as the condensed pressures $\mathbf{P_{1+2}}$ and $\mathbf{P^M_{1+2}}$ are computed from numerical models. The procedure to perform these calculations will be detailed in the following paragraphs.

Appendix B.1. Condensed impedances of the global system 1+2

To compute the condensed impedances of the infinite water medium, as the decoupling boundaries are fictitious ones, a velocity jump must be considered, as defined in Eq. (18). This velocity jump can be emulated by considering an integral formulation derived from the indirect BEM formulation. According to this formulation, the pressure field from a radiating surface can be expressed from the single layer potential due to a layer of monopole sources, representing a velocity jump at the crossing of this surface

$$p(M) = \iint_{\Omega} \nu(P) G(M,P)\, \mathrm{d}\Omega(P), \quad M \in \Omega, \quad P \in \Omega \tag{B.1}$$

with $\nu(P)$ being the single layer potential, and $G(M,P)$ the free-field Green function defined as

$$G(M,P) = -\frac{\mathrm{e}^{\mathrm{j}k^*|M-P|}}{4\pi|M-P|} \tag{B.2}$$

where $|M-P|$ is the Euclidian distance between the two points, and k^* is the complex acoustic wavenumber ($k^* = k(1-\mathrm{j}\eta)$).

According to this formulation and to the definition of the condensation functions, the condensed impedance between the incident patch j and the receiving patch i can be computed by discretizing each patch into a certain amount of points, as illustrated in Figure 11a (the black dots correspond to the patches boundaries). Then, a layer of monopole sources is placed on the discretization points of the incident patch. The condensed impedance between those patches can finally be obtained by summing up the resulting pressures at each discretization point of the receiving patch

$$Z_{1+2}^{ij} = \mathrm{j}\omega\rho \sum_{q_i=1}^{Q_i} \sum_{s_i=1}^{S_i} \sum_{q_j=1}^{Q_j} \sum_{s_j=1}^{S_j} \frac{G(\theta_{q_j}-\theta_{q_i}, \phi_{s_j}-\phi_{s_i})}{\sqrt{\Omega_j \Omega_i}} R_j^2 R_i^2 \sin\theta_{q_j} \sin\theta_{q_i} \delta\theta_j \delta\phi_j \delta\theta_i \delta\phi_i, \quad \begin{cases} \theta_{q_j} \in [\theta_{j-1}, \theta_j] \\ \phi_{s_j} \in [\phi_{j-1}, \phi_j] \\ \theta_{q_i} \in [\theta_{i-1}, \theta_i] \\ \phi_{s_i} \in [\phi_{i-1}, \phi_i] \end{cases} \tag{B.3}$$

where Q_α and S_α are the number of points in the θ and ϕ directions in patch α, respectively. Ω_α is the surface of the patch α, $\delta\theta_\alpha$ and $\delta\phi_\alpha$ are the discretization step in the θ and ϕ directions in patch α, respectively. Finally, R_α corresponds to either R_{int} or R_{ext}, depending on the location of the patch α.

A particular attention must be given to the calculation of a direct condensed impedance (i.e. when the incident and receiving patches are the same), as a singularity appears in Eq. (B.3) when the two points are confounded. To circumvent this issue, it is possible to compute this direct condensed impedance by making an analogy with the radiation impedance of a baffled circular piston having the same surface as the patch. This quantity, which corresponds to the pressure at the surface of the piston when a uniform vibrating velocity is prescribed, yields [46]

$$Z_R = Z_0 \left(1 - \frac{J_1(2k^* r_p)}{k^* r_p} - \mathrm{j}\frac{S_1(2k^* r_p)}{k^* r_p}\right) \tag{B.4}$$

where Z_0 is the acoustic impedance, r_p is the radius of the circular piston, J_1 is the Bessel function of the first kind and S_1 is the Struve function. By analogy, the impedance of a uniform velocity jump on a circular surface gives the same expression as Eq. (B.4).

Appendix B.2. Condensed pressures of the global system 1+2

For the system 1+2 (i.e. the infinite water medium), two condensed pressures must also be computed to apply Eq. (20). They correspond to the pressure induced by the given excitation (acoustic plane wave for $\mathbf{P_{1+2}}$ and monopole of unit volume velocity for $\mathbf{P^M_{1+2}}$) at the decoupling interfaces Ω_{ext} and Ω_{int}, projected on the condensation functions. In practice, they are computed numerically by evaluating their analytical expression over the discretization points of the patches (already defined in Appendix B.1), and then summing those values over the points belonging to the given patch. The condensed pressure induced by the acoustic plane wave of unit amplitude is then given by the following expression

$$P_{1+2,i} = \sum_{q_i=1}^{Q_i} \sum_{s_i=1}^{S_i} \frac{\mathrm{e}^{\mathrm{j}k^* R_i \cos\theta_{q_i}}}{\sqrt{\Omega_i}} R_i \sin\theta_{q_i} \delta\theta_i \delta\phi_i, \quad \theta_{q_i} \in [\theta_{i-1}, \theta_i] \tag{B.5}$$

and the condensed pressure induced by the monopole of unit volume velocity located at point M reads

$$P^M_{1+2,i} = \frac{\mathrm{j}\omega\rho}{4\pi\sqrt{\Omega_i}} \sum_{q_i=1}^{Q_i} \sum_{s_i=1}^{S_i} \frac{\mathrm{e}^{\mathrm{j}k^* |M - P(\theta_{q_i}, \phi_{s_i})|}}{|M - P(\theta_{q_i}, \phi_{s_i})|} R_i \sin\theta_{r_i} \delta\theta_i \delta\phi_i, \quad \begin{cases} \theta_{r_i} \in [\theta_{i-1}, \theta_i] \\ \phi_{s_i} \in [\phi_{i-1}, \phi_i] \end{cases} \tag{B.6}$$

where R_i can either be R_{ext} or R_{int} depending on the location of the patch i, and Ω_i is the surface of the patch i.

Appendix B.3. Condensed impedances of the subtracted subsystem 2

Concerning the condensed impedances of the hollow water sphere, its definition is given by Eq. (17). As it is a bounded system of relatively small size, its condensed impedances can be computed by using a Finite Element (FE) formulation. For an acoustical system, this latter yields

$$\left(\left[\mathbf{K}\right] - \omega^2 \left[\mathbf{M}\right](1 - 2\mathrm{j}\eta)\right)\{\mathbf{P}\} = \{\mathbf{Q}\} \tag{B.7}$$

where $[\mathbf{K}]$ and $[\mathbf{M}]$ are the acoustic stiffness and mass matrices, respectively, $\{\mathbf{P}\}$ is the output pressure vector, and $\{\mathbf{Q}\}$ is the input volume velocity vector.

A FE model of the hollow water sphere is built, and the nodes located at the decoupling boundaries Ω_{ext} and Ω_{int} are associated to the patch to which they belong. This is illustrated in Figure 11b, where the patches boundaries are shown on Ω_{ext} only (and not Ω_{int} in order to avoid loading too much the figure. The nodes of the FE model belonging to Ω_{int} are shown in red at the center of the sphere. To compute the condensed impedance between the incident patch j and the receiving patch i, a volume velocity excitation is applied at the N_j nodes belonging to the incident patch. The input volume velocity vector $\{\mathbf{Q^j}\}$ associated to this excitation will then have N_j non-null components Q_n^j

$$Q_n^j = \frac{\delta S_n}{\sqrt{\Omega_j}}, \quad n \in [\![1, N_j]\!] \tag{B.8}$$

where δS_n is the area around the node n, and Ω_j the surface of the patch j. The resulting pressure vector $\{\mathbf{P^j}\}$ associated to this excitation can be obtained by inverting directly the dynamic matrix of Eq. (B.7)

$$\{\mathbf{P^j}\} = \left(\left[\mathbf{K}\right] - \omega^2 \left[\mathbf{M}\right](1 - 2\mathrm{j}\eta)\right)^{-1}\{\mathbf{Q^j}\} \tag{B.9}$$

Then, similarly to the calculation of $\mathbf{Z_{1+2}}$, the condensed impedance between the two patches is obtained by summing up the resulting pressures at the M_i nodes belonging to the receiving patch

$$Z_2^{ij} = \frac{1}{\sqrt{\Omega_i}} \sum_{m=1}^{M_i} P_m^j \delta S_m \tag{B.10}$$

where P_m^j is the pressure at node m belonging to the patch i when the system is excited on the patch j, δS_m is the area around the node m, and Ω_i is the surface of the patch i.

References

[1] W. C. Hurty, Dynamic analysis of structural systems using component modes, AIAA Journal 3 (4) (1965) 678–685. doi:10.2514/3.2947.

[2] R. R. Craig, M. C. C. Bampton, Coupling of substructures for dynamic analyses., AIAA Journal 6 (7) (1968) 1313–1319. doi:10.2514/3.4741.

[3] G. M. L. Gladwell, Branch mode analysis of vibrating systems, J. Sound Vib. 1 (1) (1964) 41–59. doi:10.1016/0022-460X(64)90006-9.

[4] D. J. Rixen, A dual Craig–Bampton method for dynamic substructuring, J. Comput. Appl. Math. 168 (1-2) (2004) 383–391. doi:10.1016/j.cam.2003.12.014.

[5] R. MacNeal, A hybrid method of component mode synthesis, Comput. Struct. 1 (4) (1971) 581–601. doi:10.1016/0045-7949(71)90031-9.

[6] R. H. Lyon, G. Maidanik, Power flow between linearly coupled oscillators, J. Acoust. Soc. Am. 34 (5) (1962) 623–639. doi:10.1121/1.1918177.

[7] A. Le Bot, V. Cotoni, Validity diagrams of statistical energy analysis, J. Sound Vib. 329 (2) (2010) 221–235. doi:10.1016/j.jsv.2009.09.008.

[8] H. Li, N. Totaro, L. Maxit, A. Le Bot, Ergodic billiard and statistical energy analysis, Wave Motion 87 (2019) 166–178. doi:10.1016/j.wavemoti.2018.08.011.

[9] F. Firestone, The mobility method of computing the vibration of linear mechanical and acoustical systems: mechanical-electrical analogies, J. Appl. Phys. 9 (6) (1938) 373–387. doi:10.1063/1.1710432.

[10] S. Rubin, Transmission matrices for vibration and their relation to admittance and impedance, J. Eng. Ind. 86 (1) (1964) 9–21. doi:10.1115/1.3670463.

[11] G. O'Hara, Mechanical impedance and mobility concepts, J. Acoust. Soc. Am. 41 (5) (1967) 1180–1184. doi:10.1121/1.1910456.

[12] R. Bishop, D. Johnson, The mechanics of vibration, Cambridge University Press, Cambridge, UK, 1979.

[13] B. Petersson, J. Plunt, On effective mobilities in the prediction of structure-borne sound transmission between a source structure and a receiving structure, part II: Procedures for the estimation of mobilities, J. Sound Vib. 82 (4) (1982) 531–540. doi:10.1016/0022-460X(82)90406-0.

[14] B. Petersson, J. Plunt, On effective mobilities in the prediction of structure-borne sound transmission between a source structure and a receiving structure, part I: Theoretical background and basic experimental studies, J. Sound Vib. 82 (4) (1982) 517–529. doi:10.1016/0022-460X(82)90405-9.

[15] S. Kim, M. Brennan, A compact matrix formulation using the impedance and mobility approach for the analysis of structural-acoustic systems, J. Sound Vib. 223 (1) (1999) 97–113. doi:10.1006/jsvi.1998.2096.

[16] M. Ouisse, L. Maxit, C. Cacciolati, J.-L. Guyader, Patch transfer function as a tool to couple linear acoustic problems, J. Vib. Acoust. 127 (2005) pp. 458–466.

[17] G. Veronesi, C. Albert, E. Nijman, J. Rejlek, A. Bocquillet, Patch transfer function approach for analysis of coupled vibro-acoustic problems involving porous materials, in: SAE Technical Paper, Graz, Austria, 2014, pp. 2014–01–2092. doi:10.4271/2014-01-2092.

[18] J.-D. Chazot, J.-L. Guyader, Prediction of transmission loss of double panels with a patch-mobility method, J. Acoust. Soc. Am. 121 (1) (2007) 267–278. doi:10.1121/1.2395920.

[19] J.-D. Chazot, J.-L. Guyader, Transmission loss of double panels filled with porogranular materials, J. Acoust. Soc. Am. 126 (6) (2009) 3040–3048. doi:10.1121/1.3245033.

[20] L. Maxit, C. Yang, L. Cheng, J.-L. Guyader, Modeling of micro-perforated panels in a complex vibro-acoustic environment using patch transfer function approach, J. Acoust. Soc. Am. 131 (3) (2012) 2118–2130. doi:10.1121/1.3682055.

[21] X. Yu, L. Cheng, J.-L. Guyader, Modeling vibroacoustic systems involving cascade open cavities and micro-perforated panels, J. Acoust. Soc. Am. 136 (2) (2014) 659–670. doi:10.1121/1.4887442.

[22] X. Zhang, L. Cheng, Acoustic silencing in a flow duct with micro-perforated panel liners, Appl. Acoust. 167 (2020) 107382. doi:10.1016/j.apacoust.2020.107382.

[23] M. Aucejo, L. Maxit, N. Totaro, J.-L. Guyader, Convergence acceleration using the residual shape technique when solving structure–acoustic coupling with the Patch Transfer Functions method, Comput. Struct. 88 (11) (2010) 728–736. doi:10.1016/j.compstruc.2010.02.010.

[24] L. Maxit, M. Aucejo, J.-L. Guyader, Improving the Patch Transfer Function approach for fluid-structure modelling in heavy fluid, J. Vib. Acoust. 134 (5) (2012) 051011. doi:10.1115/1.4005838.

[25] V. Meyer, L. Maxit, J.-L. Guyader, T. Leissing, C. Audoly, A condensed transfer function method as a tool for solving vibroacoustic problems, Proceedings of the Institution of Mechanical Engineers, Part C: Journal of Mechanical Engineering Science 230 (6) (2016) 928–938. doi:10.1177/0954406215615627.

[26] L. Maxit, J.-M. Ginoux, Prediction of the vibro-acoustic behavior of a submerged shell non periodically stiffened by internal frames, J. Acoust. Soc. Am. 128 (1) (2010) 137–151. doi:10.1121/1.3436526.

[27] V. Meyer, L. Maxit, J.-L. Guyader, T. Leissing, Prediction of the vibroacoustic behavior of a submerged shell with non-axisymmetric internal substructures by a condensed transfer function method, J. Sound Vib. 360 (2016) 260–276. doi:10.1016/j.jsv.2015.09.030.

[28] V. Meyer, L. Maxit, C. Audoly, A substructuring approach for modeling the acoustic scattering from stiffened submerged shells coupled to non-axisymmetric internal structures, J. Acoust. Soc. Am. 140 (3) (2016) 1609–1617. doi:10.1121/1.4962235.

[29] Z. Hu, L. Maxit, L. Cheng, Piecewise convergence behavior of the condensed transfer function approach for mid-to-high frequency modelling of a panel-cavity system, J. Sound Vib. 435 (2018) 119–134. doi:10.1016/j.jsv.2018.08.010.

[30] Z. Hu, L. Maxit, L. Cheng, Acoustic design and analyses of a double Skin Façade system, Appl. Acoust. 173 (2021) 107727. doi:10.1016/j.apacoust.2020.107727.

[31] D. T. Soedel, W. Soedel, Synthesizing reduced systems by complex receptances, J. Sound Vib. 179 (5) (1994) 855 – 867. doi:https://doi.org/10.1006/jsvi.1995.0057.

[32] D. T. Huang, E. C. Ting, Vibration of plates with sub-structural deduction: a reverse receptance approach, J. Sound Vib. 271 (1-2) (2004) 177–207. doi:10.1016/S0022-460X(03)00368-7.

[33] D. T. Huang, Effects of constraint, circular cutout and in-plane loading on vibration of rectangular plates, Int. J. Mech. Sci. 68 (2013) 114–124. doi:10.1016/j.ijmecsci.2013.01.005.

[34] D. T. Huang, A reverse receptance approach for analysis of vibration of grooved plates, Int. J. Mech. Sci. 53 (12) (2011) 1084–1102. doi:10.1016/j.ijmecsci.2011.09.003.

[35] W. D'Ambrogio, A. Fregolent, Prediction of the substructure properties using decoupling procedures, in: Structural Dynamics - Eurodyn 2005, Proceedings of the 6th International Conference on Structural Dynamics, Paris, France, 2005, p. 8.

[36] W. D'Ambrogio, A. Fregolent, Promises and pitfalls of decoupling procedures, in: 26th IMAC: Conference and Exposition on Structural Dynamics, Orlando, USA, 2008, p. 8.

[37] W. D'Ambrogio, A. Fregolent, The role of interface DoFs in decoupling of substructures based on the dual domain decomposition, Mech. Syst. Signal Pr. 24 (7) (2010) 2035–2048. doi:10.1016/j.ymssp.2010.05.007.

[38] S. Voormeeren, D. Rixen, A family of substructure decoupling techniques based on a dual assembly approach, Mech. Syst. Signal Pr. 27 (2012) 379–396. doi:10.1016/j.ymssp.2011.07.028.

[39] O. Tuysuz, Y. Altintas, Frequency domain updating of thin-walled workpiece dynamics using reduced order substructuring method in machining, J. Manuf. Sci. E-T. Asme 139 (7) (2017) 071013. doi:10.1115/1.4036124.

[40] F. Dumortier, L. Maxit, V. Meyer, Vibroacoustic subtractive modeling using a reverse condensed transfer function approach, J. Sound Vib. 499 (2021) 115982. doi:10.1016/j.jsv.2021.115982.

[41] F. Dumortier, L. Maxit, V. Meyer, Subtractive modelling using the reverse condensed transfer function method: influence of the numerical errors, in: Proceedings of InterNoise 2021, Washington DC, USA, 2021, p. 12.

[42] F. J. Fahy, Some applications of the reciprocity principle in experimental vibroacoustics, Acoust. Phys. 49 (2) (2003) 217–229. doi:10.1134/1.1560385.

[43] D. J. Higham, Condition numbers and their condition numbers, Linear Algebra Appl. 214 (1995) 193–213. doi:10.1016/0024-3795(93)00066-9.

[44] M. C. Junger, D. Feit, Sound, structures, and their interaction, Vol. 225, MIT press Cambridge, MA, Cambridge, USA, 1986.

[45] J.-L. Guyader, Vibration des milieux continus [Vibration in continuous media], Hermes Sciences, Paris, France, 2002.

[46] T. Valier-Brasier., Rayonnement acoustique [Acoustic radiation], Université Pierre et Marie Curie, Paris, France, 2017.